S1 Basal ice speed and basal drag map

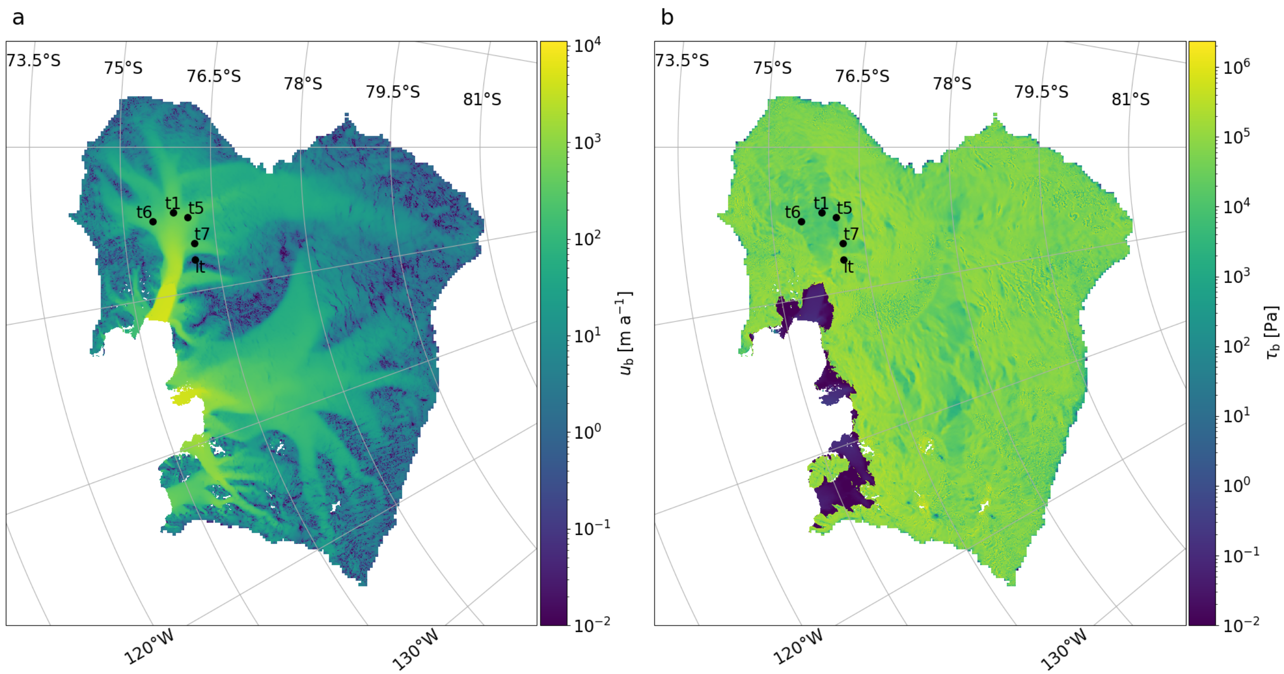

Figure S1. Basal sliding speed (a) and basal shear stress (b) in the Amundsen Sea Embayment retrieved from the surface-to-bed inversion. The black dots mark the locations of the seismic observation sites.

S2 Posterior probabilities when using sub-sampled data

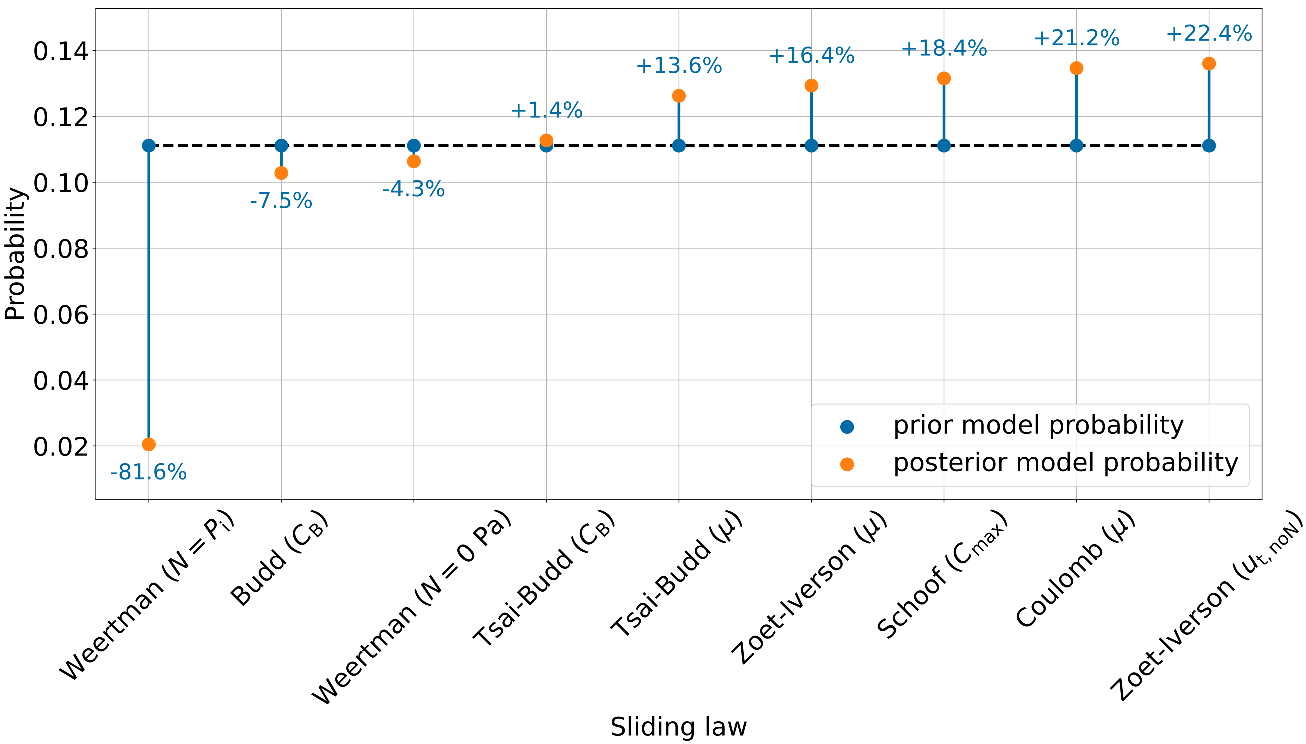

Figure S2. Normalized probabilities when using only every 10th acoustic impedance measurement collected on Pine Island Glacier (PIG). Otherwise, as Fig. 6 in the main text.

S3 Metrics involved in determining the acoustic impedance misfit

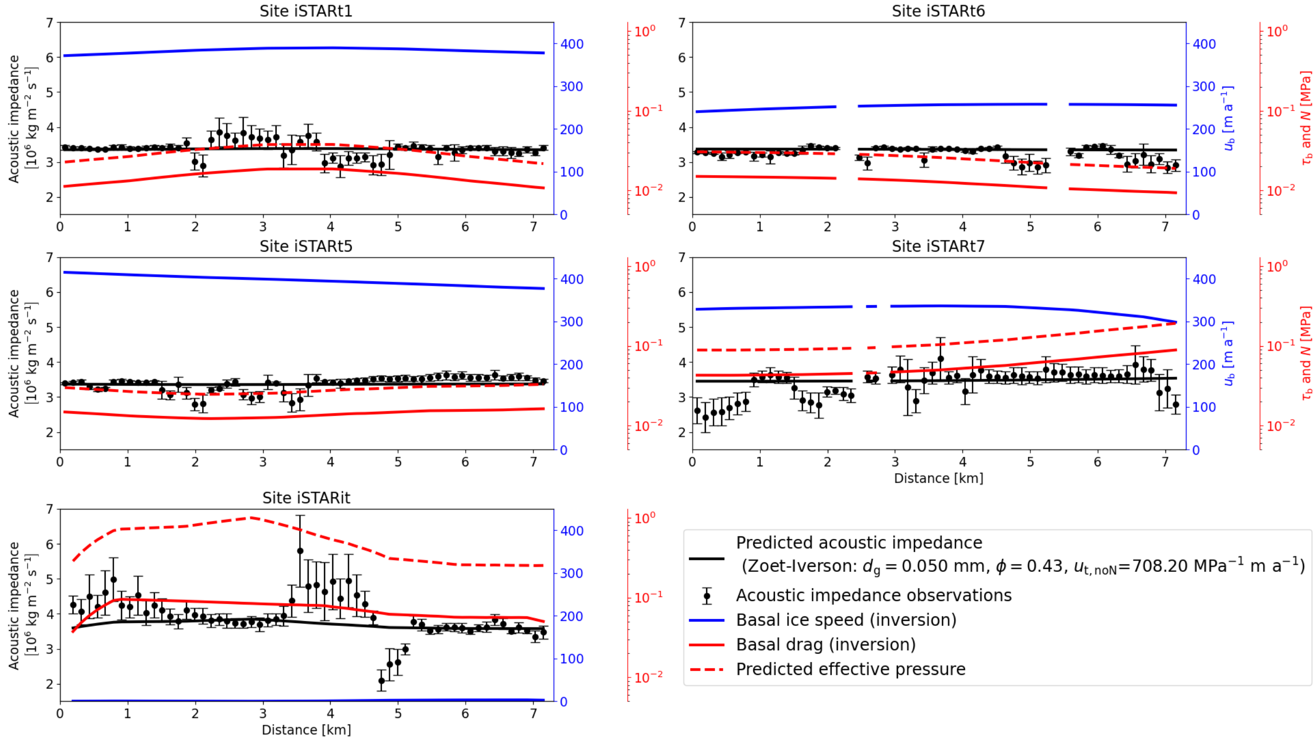

Figure S3. Metrics involved in predicting the acoustic impedance based on the Viscous Grain-Shearing (VGS) theory and calculating the misfit to the seismic observations. The black, blue, and red colours (lines, points, and axes) represent acoustic impedance, basal ice speed, and basal drag and effective pressure, respectively. The results are based on the Zoet-Iverson $(u_{\mathrm{t,noN}})$ sliding law with the maximum a posterior (MAP) parameter values. μ was fixed at 0.5.

S4 Prior distribution – Maximum up-slope angle of the bed and Iken's bound

The distribution of the up-slope angles of the bed in flow direction (β) and the corresponding Iken's bound ($C_{\max} = \tan\beta$; Fig. S4) is examined for the center part of Pine Island Glacier (PIG; magenta box in Fig. S5). As the horizontal grid resolution of Bedmap2 is $1\ \mathrm{km}$ Fretwell et al. (2013)), the maximum up-slope angle (and therefore $C_{\max}$) on smaller scales might be significantly larger than suggested by the distribution in Fig. S4. For example, autonomous underwater vehicle (AUV) data collected downstream of Thwaites Glacier ($1.5\ \mathrm{m}$ horizontal resolution; Graham et al., 2022) and under the Thwaites Eastern Ice Shelf ($2\ \mathrm{m}$ horizontal resolution; Wåhlin, unpublished data) indicate that the maximum $C_{\max} > 0.7$ (largest value tested within this study; Fig. S6). However, as the horizontal resolution of the inversion used to derive the basal shear stress and sliding speed is much coarser ($1\ \mathrm{km}$; same as the Bedmap2 resolution), it is not straightforward to determine the $C_{\max}$ prior directly from the AUV data. Nevertheless, the chosen $C_{\max}$ prior aims to incorporate higher bed angles at smaller scales through a more gradual decline towards higher values while aligning the highest probability with the extreme values in Fig. S4.

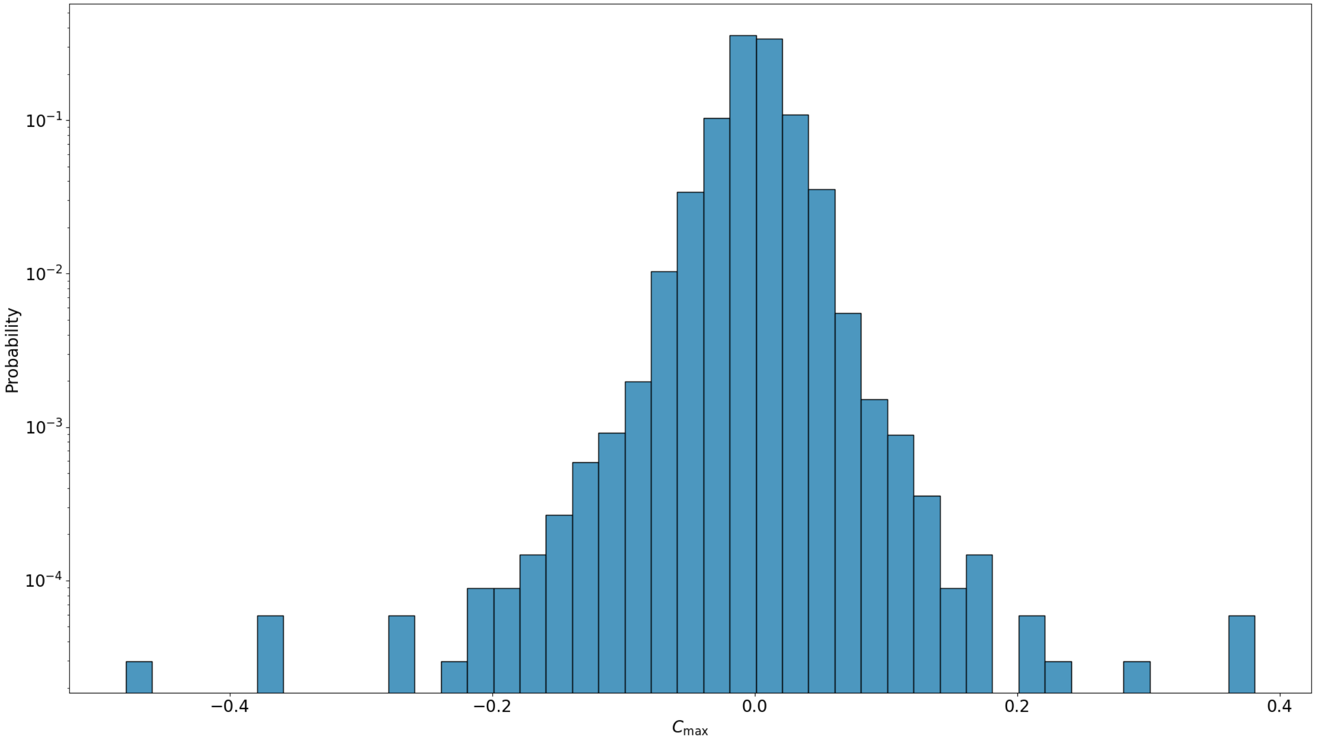

Figure S4. $C_{\max}$ distribution in flow direction within the magenta box in Fig. S5. The Bedmap2 horizontal grid resolution is $1\ \mathrm{km}$ (Fretwell et al., 2013). The bin width is 0.02.

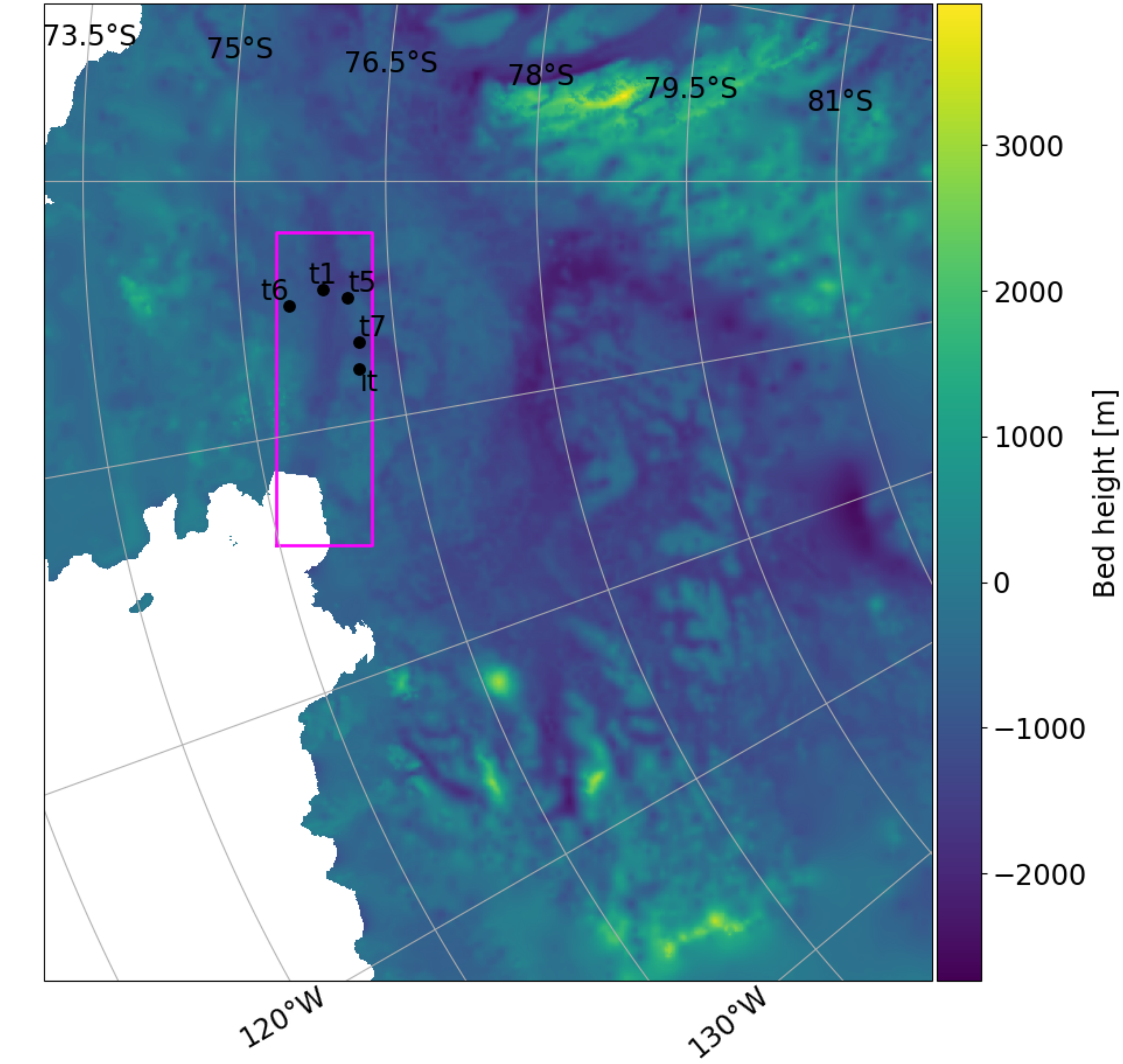

Figure S5. Bed height for areas with ice cover (grounded and floating; based on Bedmap2; Fretwell et al., 2013). The magenta box frames the main trunk of Pine Island Glacier (PIG) and the black dots mark the locations of the acoustic impedance data sites.

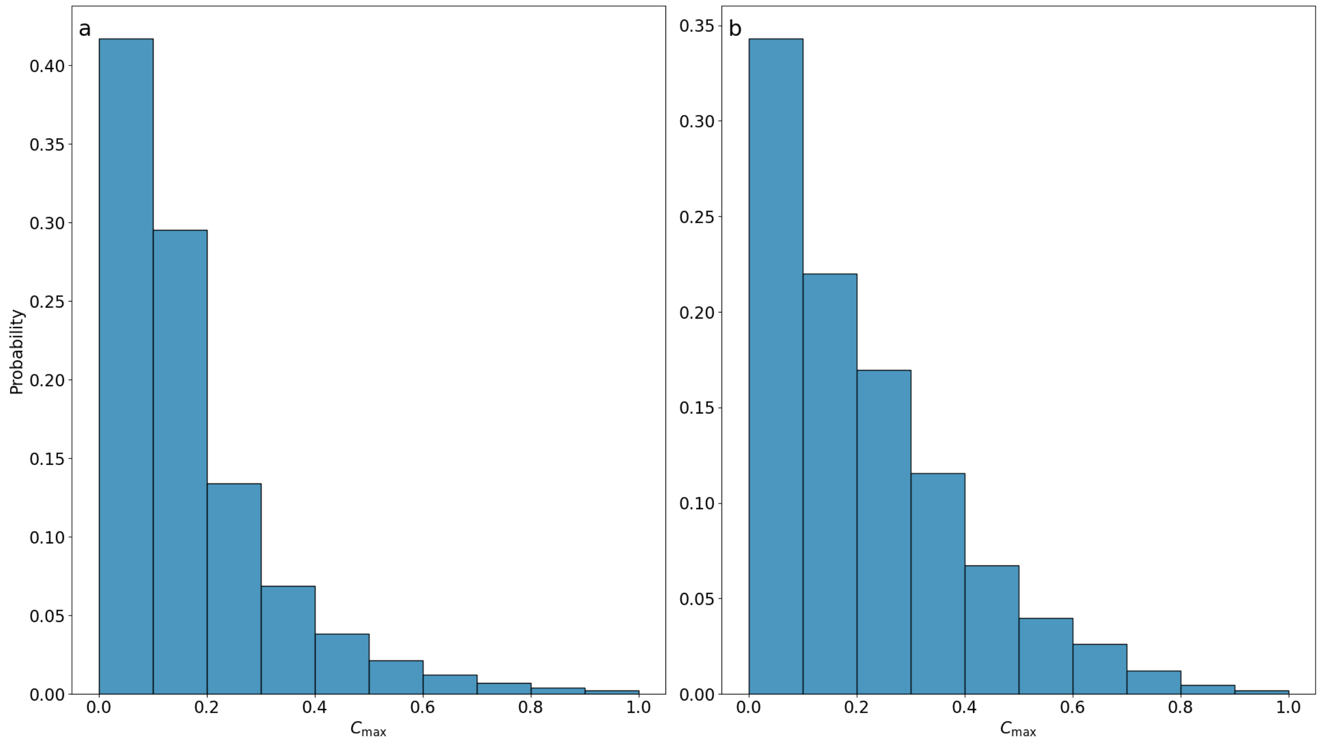

Figure S6. C_{max} distribution from autonomous underwater vehicle (AUV) data collected downstream of Thwaites Glacier (a; 1.5 m horizontal resolution; Graham et al., 2022) and under the Thwaites Eastern Ice Shelf (b; 2 m horizontal resolution; Wåhlin, unpublished data). The bin width is 0.1. C_{max} values > 1.0 are not shown here. The corresponding spatial distributions are shown in Fig. S7.

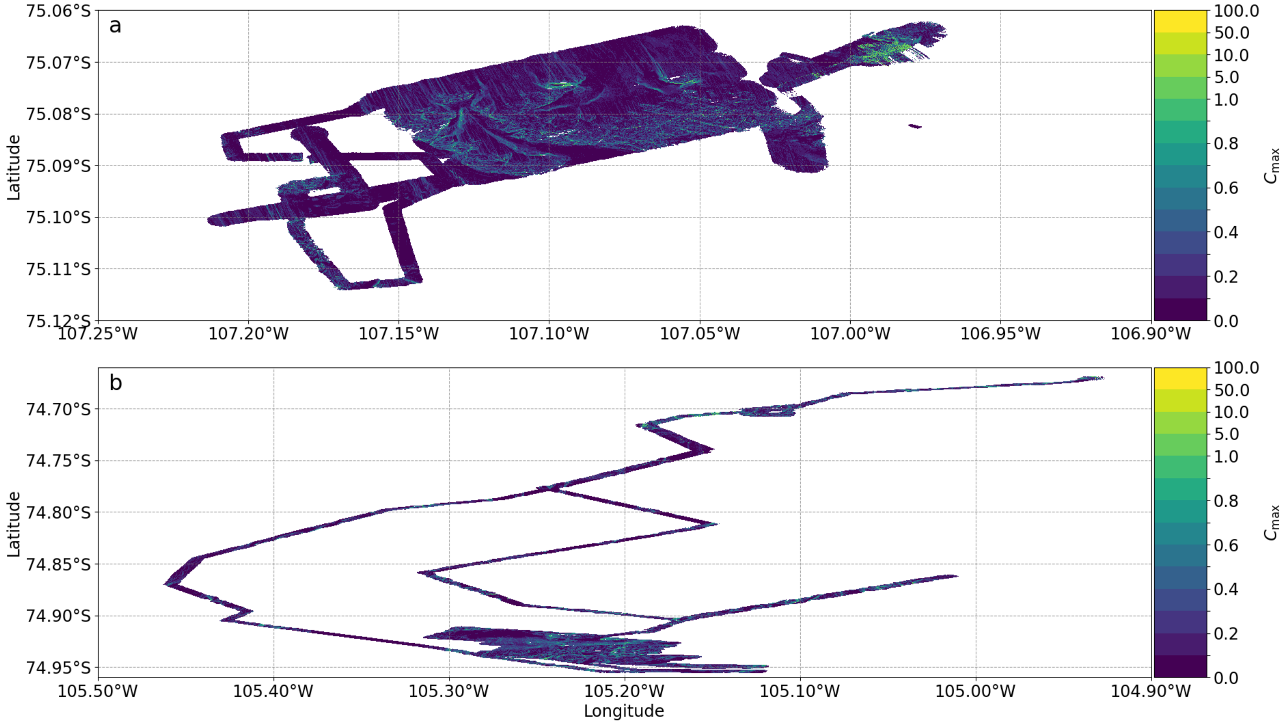

Figure S7. Spatial distribution of the autonomous underwater vehicle (AUV) data shown in Fig. S6. Note the change in colorbar step at $C_{\max} = 1.0$.

S5 Acoustic impedance data-model misfit under different sliding laws

S5.1 Weertman (endmember scenarios $N = 0$ Pa and $N = p_\mathrm{i}$)

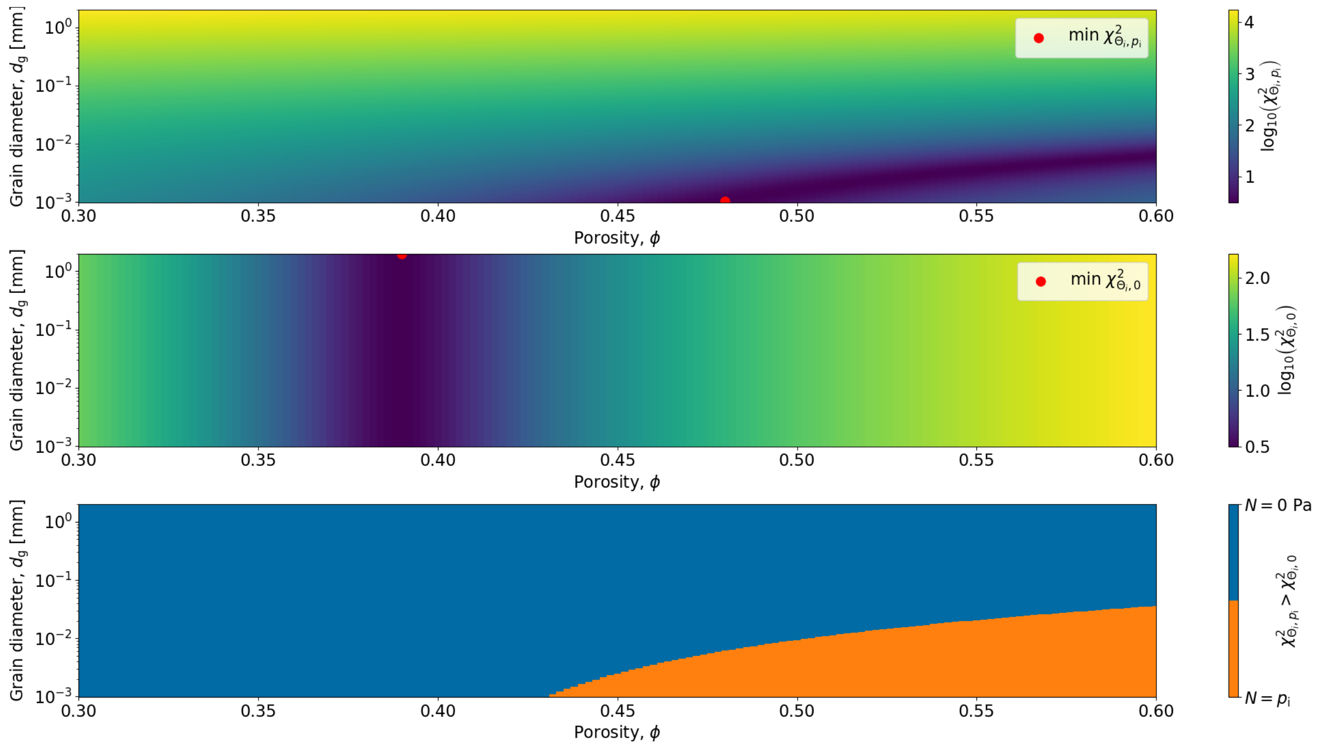

Figure S8. Variations of the misfit $\chi^2_{\Theta_i}$ with the two model parameters grain diameter (d_g) and porosity (ϕ) under the Weertman-type endmember scenarios $N = p_\mathrm{i}$ (top panel) and $N = 0$ Pa (center panel). The bottom panel shows the preferred sliding law within the parameter space. The red dots mark the minimum misfit.

S5.2 Budd (C_B)

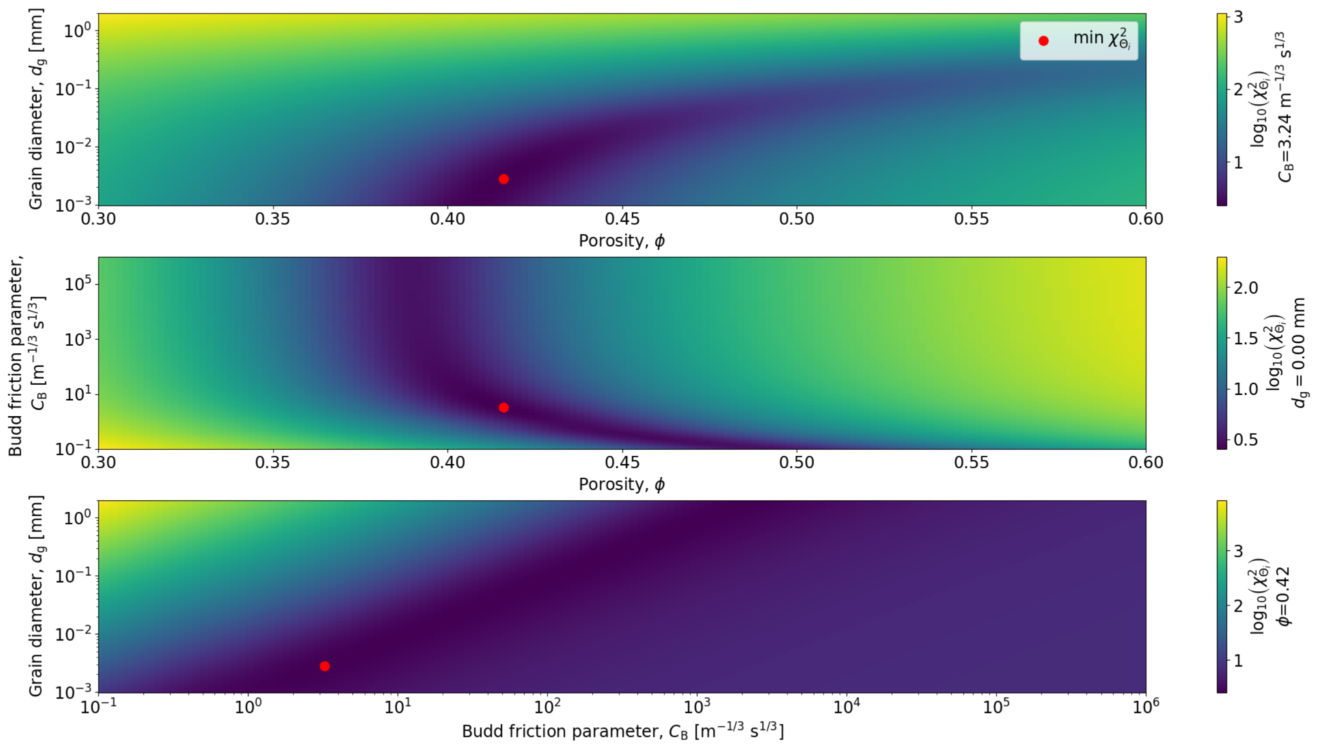

Figure S9. Variations of the misfit $\chi^2_{\Theta_i}$ with the three model parameters grain diameter (d_g), porosity (ϕ), and Budd friction parameter (C_B) under a Budd sliding law. For the parameter not shown, the value yielding the minimum misfit is used and denoted next to the colorbar of the corresponding panel. The red dots mark the minimum misfit.

S5.3 Coulomb (μ)

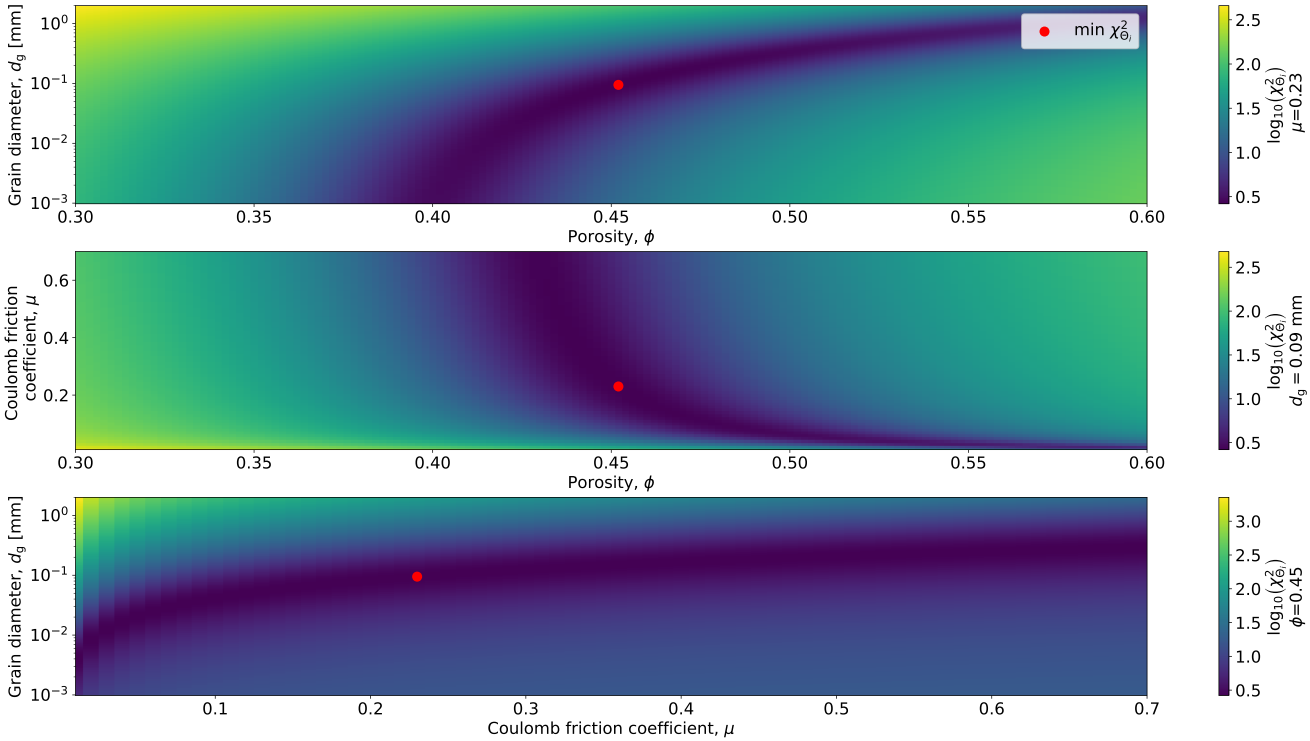

Figure S10. Variations of the misfit $\chi^2_{\Theta_i}$ with the three model parameters grain diameter (d_g), porosity (ϕ), and Coulomb friction coefficient (μ) under a Coulomb sliding law. Otherwise as Fig. S9.

S5.4 Tsai-Budd (C_B)

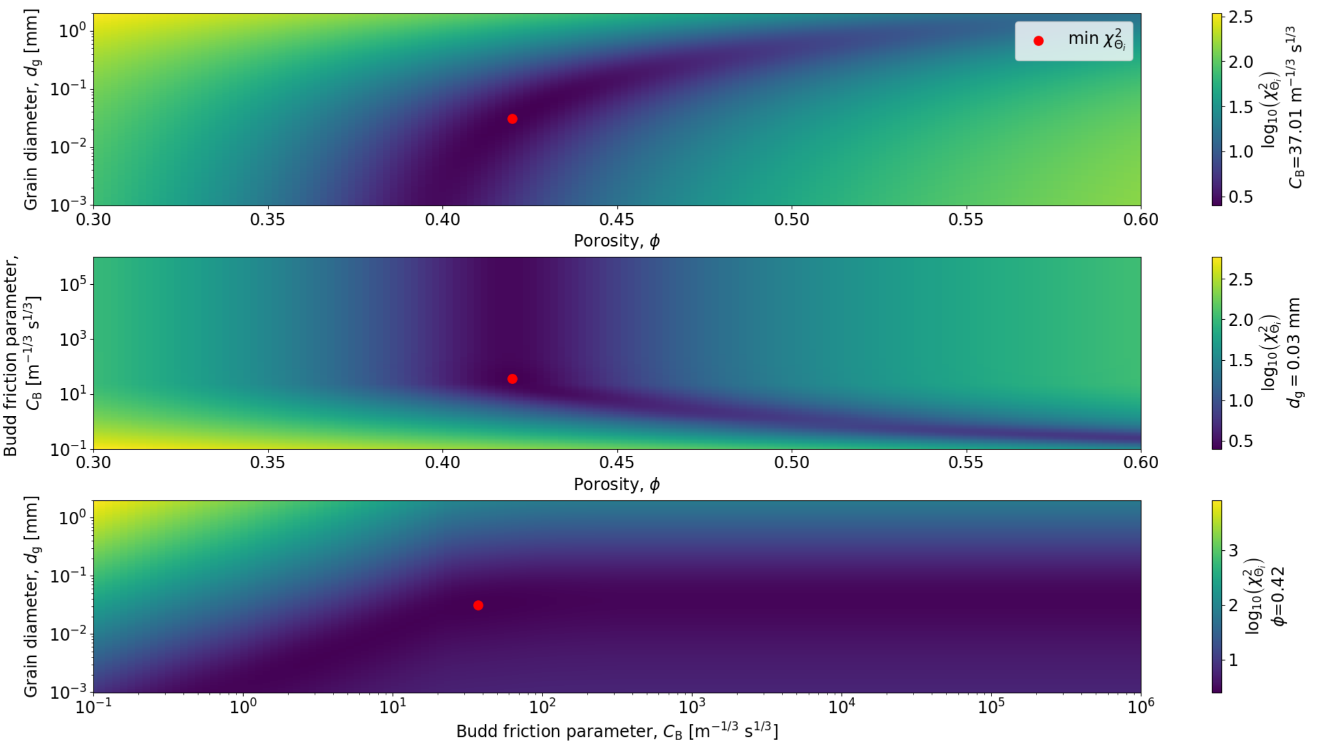

Figure S11. Variations of the misfit $\chi^2_{\Theta_i}$ with the three model parameters grain diameter (d_g), porosity (ϕ), and Budd friction parameter (C_B) under a Tsai-Budd sliding law (μ fixed at 0.5). Otherwise as Fig. S9.

20 S5.5 Tsai-Budd (μ)

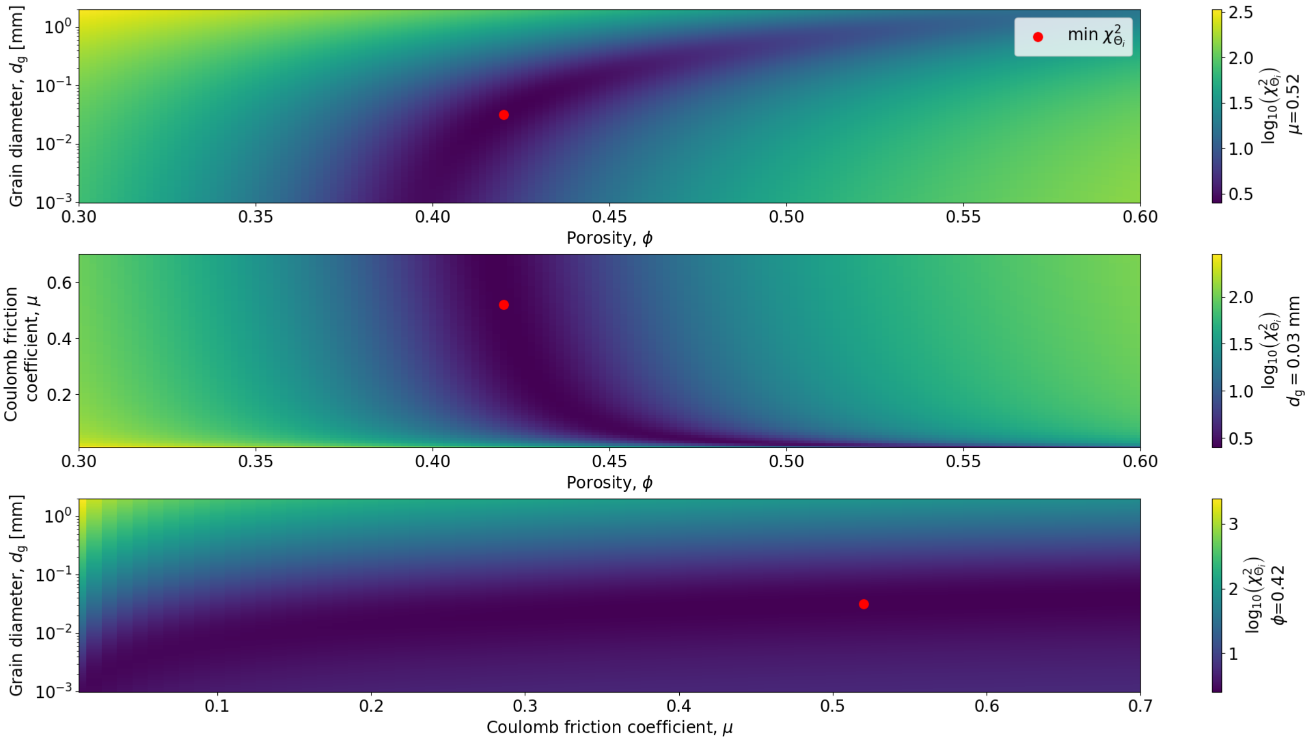

Figure S12. Variations of the misfit $\chi^2_{\Theta_i}$ with the three model parameters grain diameter (d_g), porosity (ϕ), and Coulomb friction coefficient (μ) under a Tsai-Budd sliding law (C_B fixed at $37.01\ \mathrm{m}^{-1/3}\ \mathrm{s}^{1/3}$). Otherwise as Fig. S9.

S5.6 Schoof (C_S)

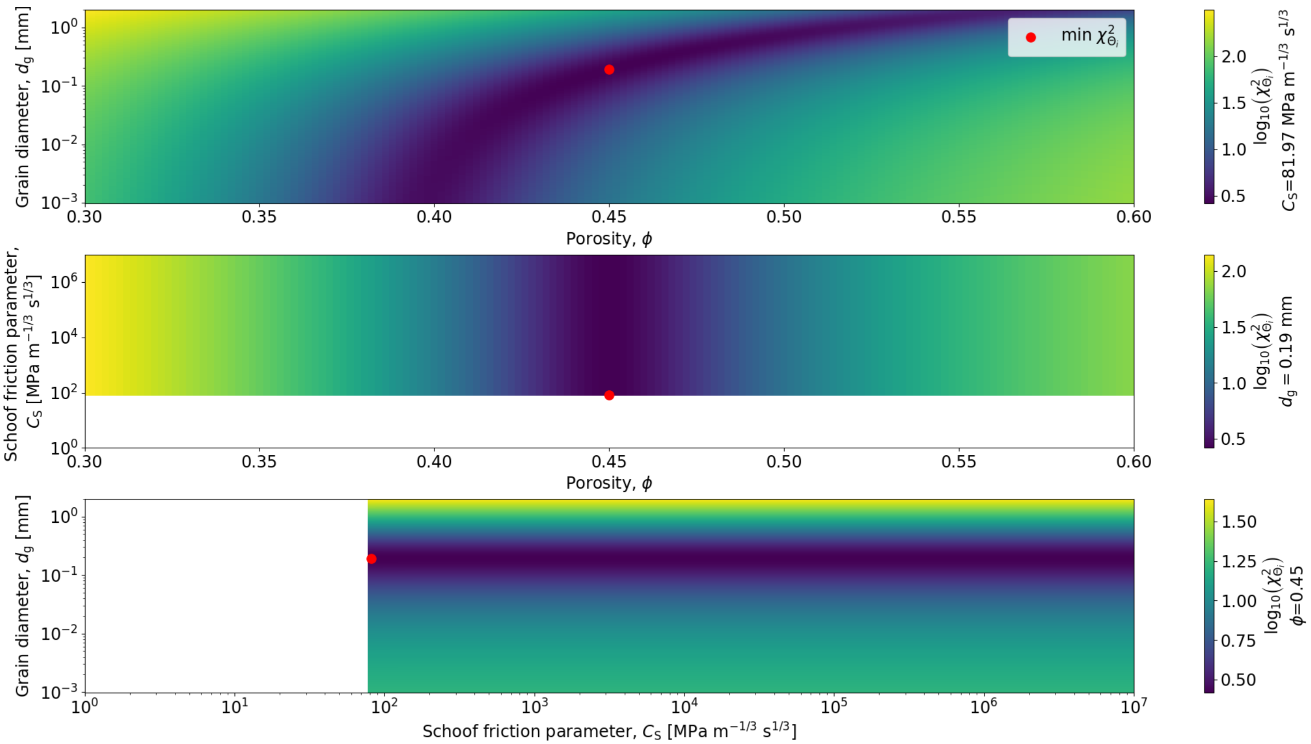

Figure S13. Variations of the misfit $\chi^2_{\Theta_i}$ with the three model parameters grain diameter (d_g), porosity (ϕ), and Schoof friction parameter (C_S) under a Schoof sliding law (C_max fixed at 0.5). The determination of $\chi^2_{\Theta_i}$ is only possible when the number of incompatible u_b−τ_b pairs is small (Fig. S14). Otherwise as Fig. S9.

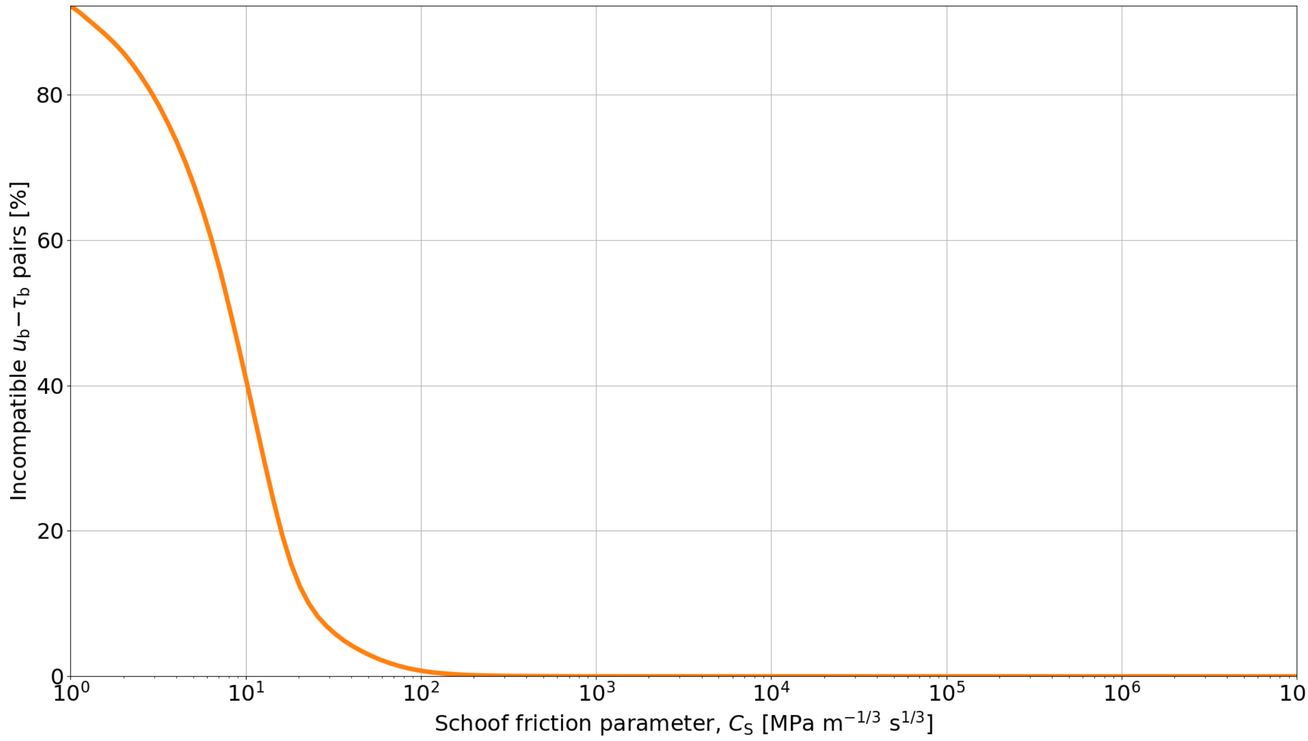

Figure S14. Percentage of incompatible $u_\mathrm{b}-\tau_\mathrm{b}$ pairs under a Schoof sliding law when varying the Schoof friction parameter (C_S; C_max fixed at 0.5).

S5.7 Schoof ($C_{\max}$)

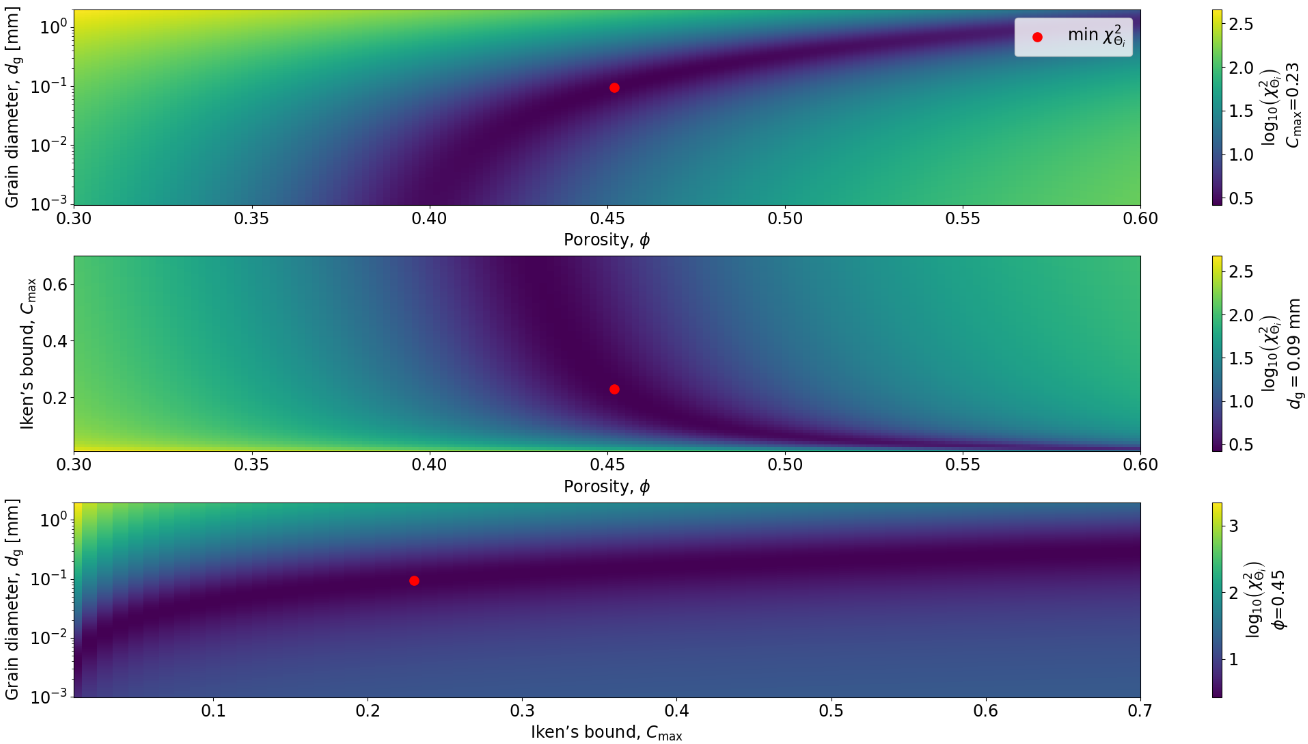

Figure S15. Variations of the misfit $\chi^2_{\Theta_i}$ with the three model parameters grain diameter (d_{g}), porosity (ϕ), and Iken's bound ($C_{\max}$) under a Schoof sliding law (C_{S} fixed at $1 \cdot 10^3$ $\mathrm{MPa\,m^{-1/3}\,s^{1/3}}$). Otherwise as Fig. S9.

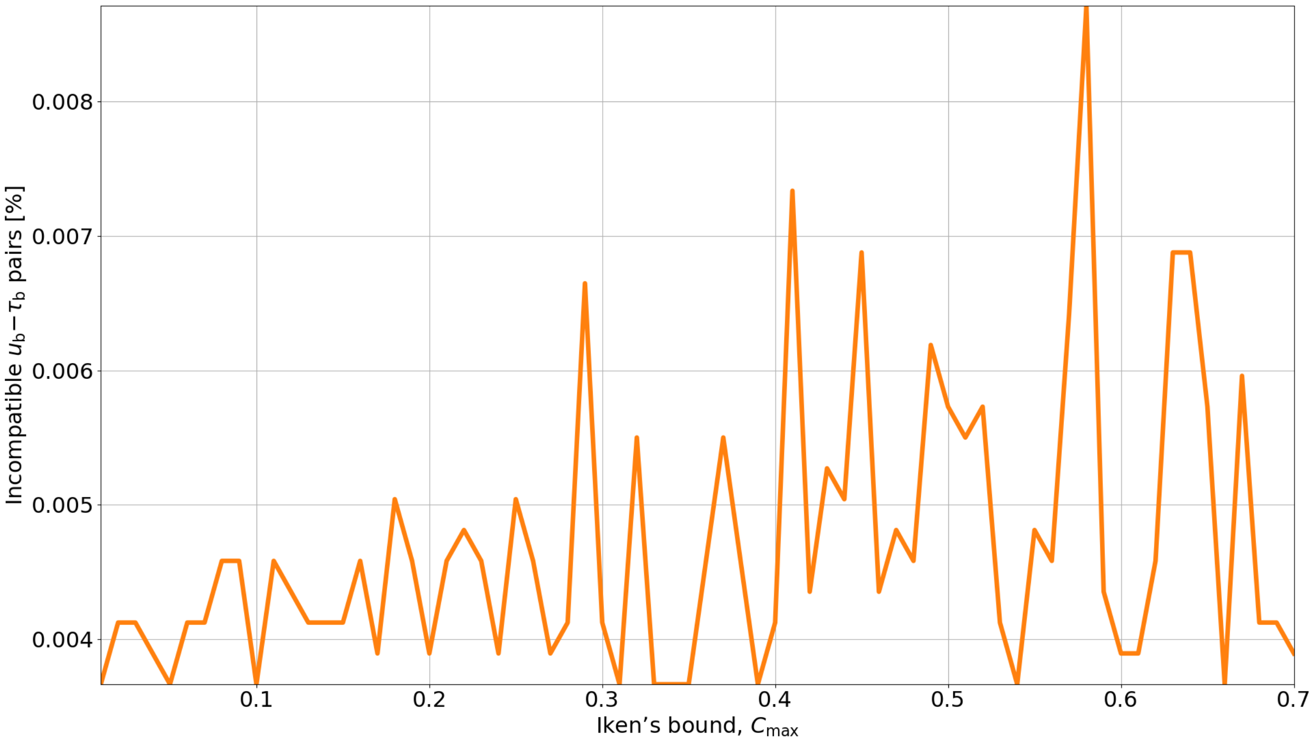

Figure S16. Percentage of incompatible $u_\mathrm{b}-\tau_\mathrm{b}$ pairs under a Schoof sliding law when varying Iken's bound (C_max; C_S fixed at $1 \cdot 10^3\ \mathrm{MPa\,m^{-1/3}\,s^{1/3}}$).

S5.8 Zoet-Iverson (μ)

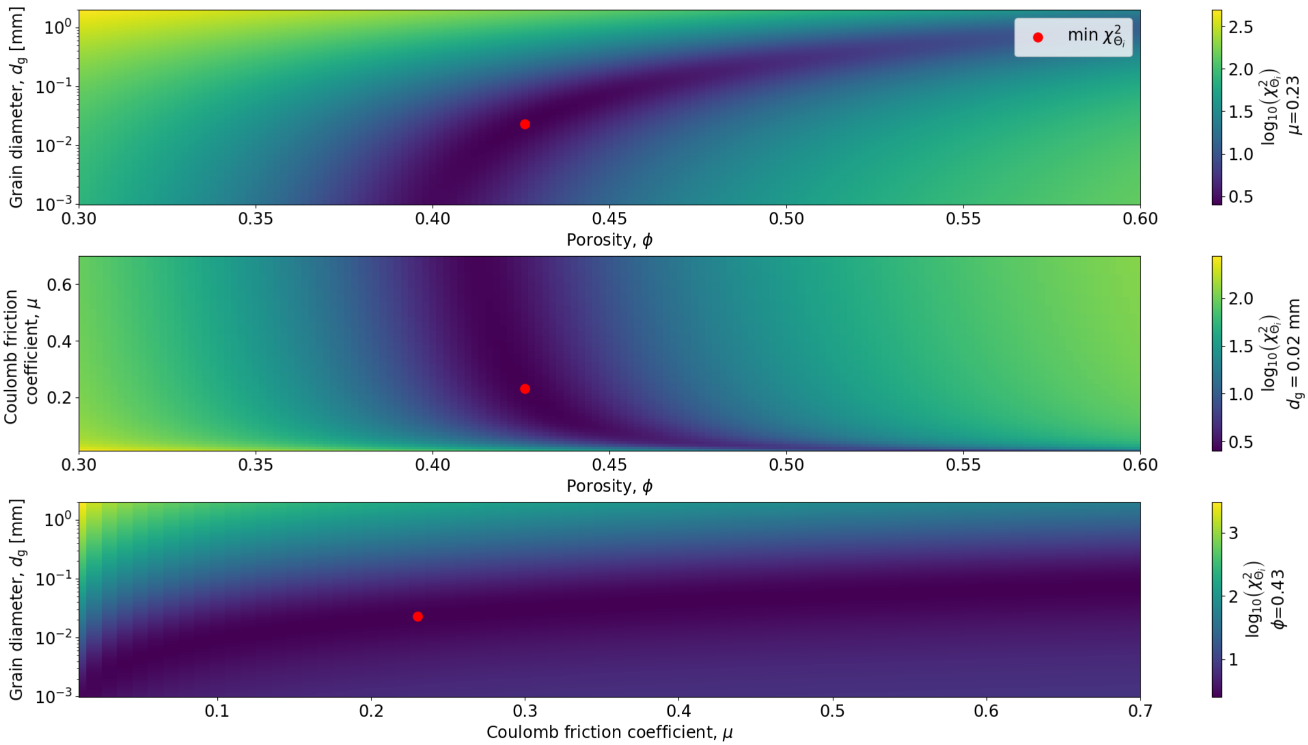

Figure S17. Variations of the misfit $\chi^2_{\Theta_i}$ with the three model parameters grain diameter (d_g), porosity (ϕ), and Coulomb friction coefficient (μ) under a Zoet-Iverson sliding law ($u_{\mathrm{t,noN}}$ fixed at $\sim 333\ \mathrm{MPa}^{-1}\ \mathrm{m\ a}^{-1}$). Otherwise as Fig. S9.

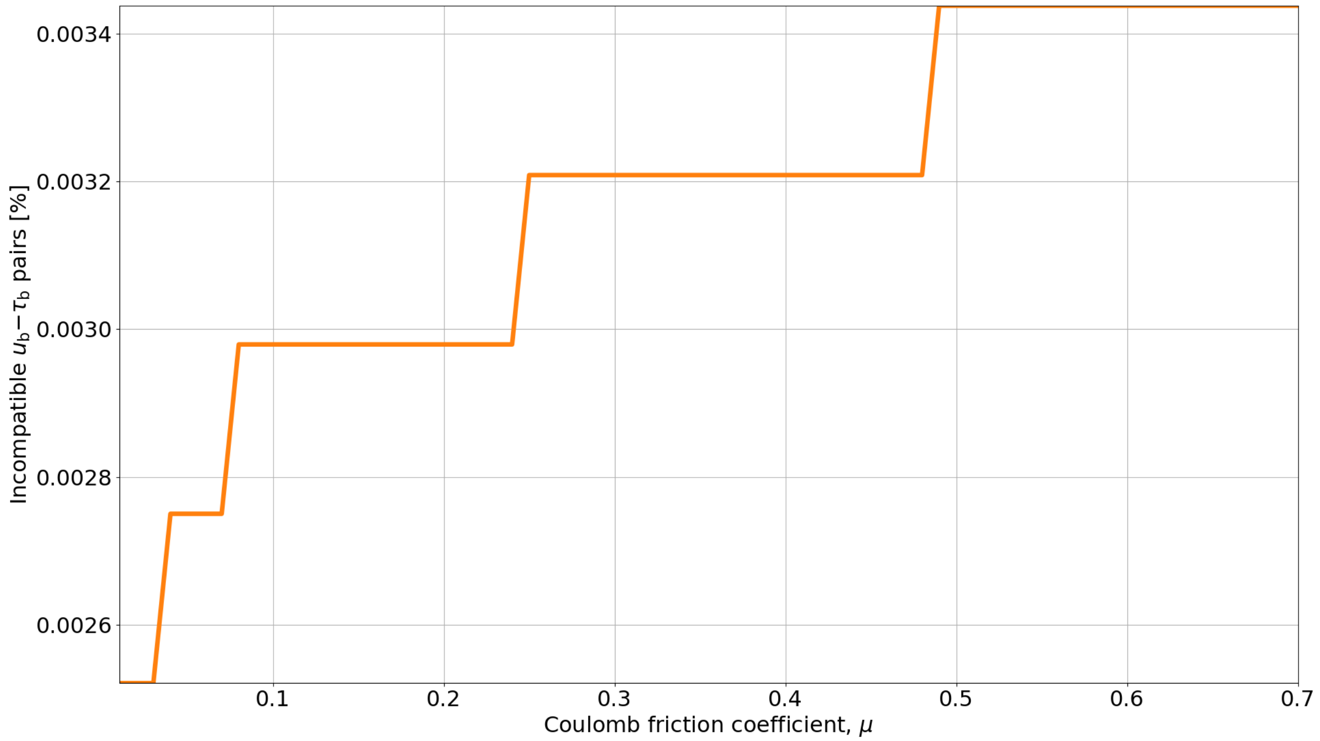

Figure S18. Percentage of incompatible $u_{\mathrm{b}}-\tau_{\mathrm{b}}$ pairs under a Zoet-Iverson sliding law when varying the Coulomb friction coefficient (μ; $u_{\mathrm{t,noN}}$ fixed at $\sim 333\ \mathrm{MPa}^{-1}\ \mathrm{m\ a}^{-1}$).

S5.9 Zoet-Iverson ($u_{\mathrm{t,noN}}$)

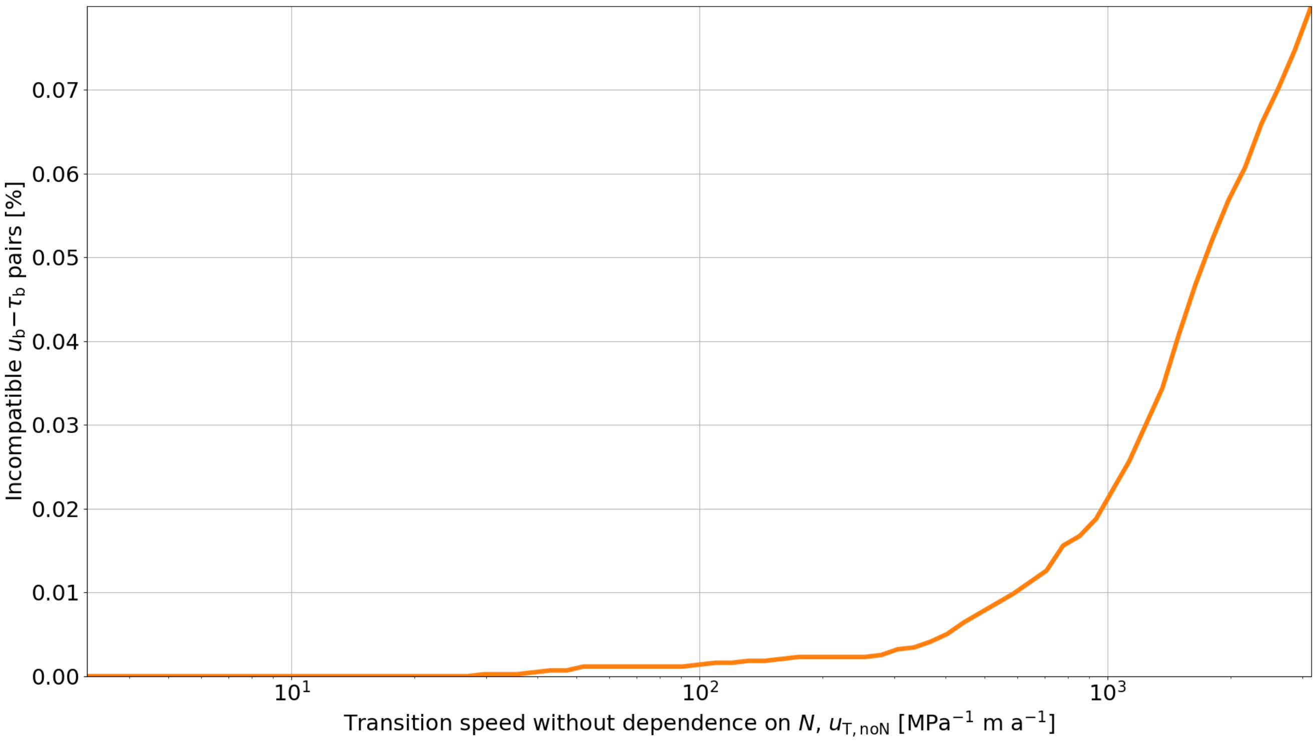

Figure S19. Percentage of incompatible $u_{\mathrm{b}}-\tau_{\mathrm{b}}$ pairs under a Zoet-Iverson sliding law when varying the transition speed without the dependence on N ($u_{\mathrm{t,noN}}$; μ fixed at 0.5).

S6 Posterior probabilities when using different fractions of the overburden pressure

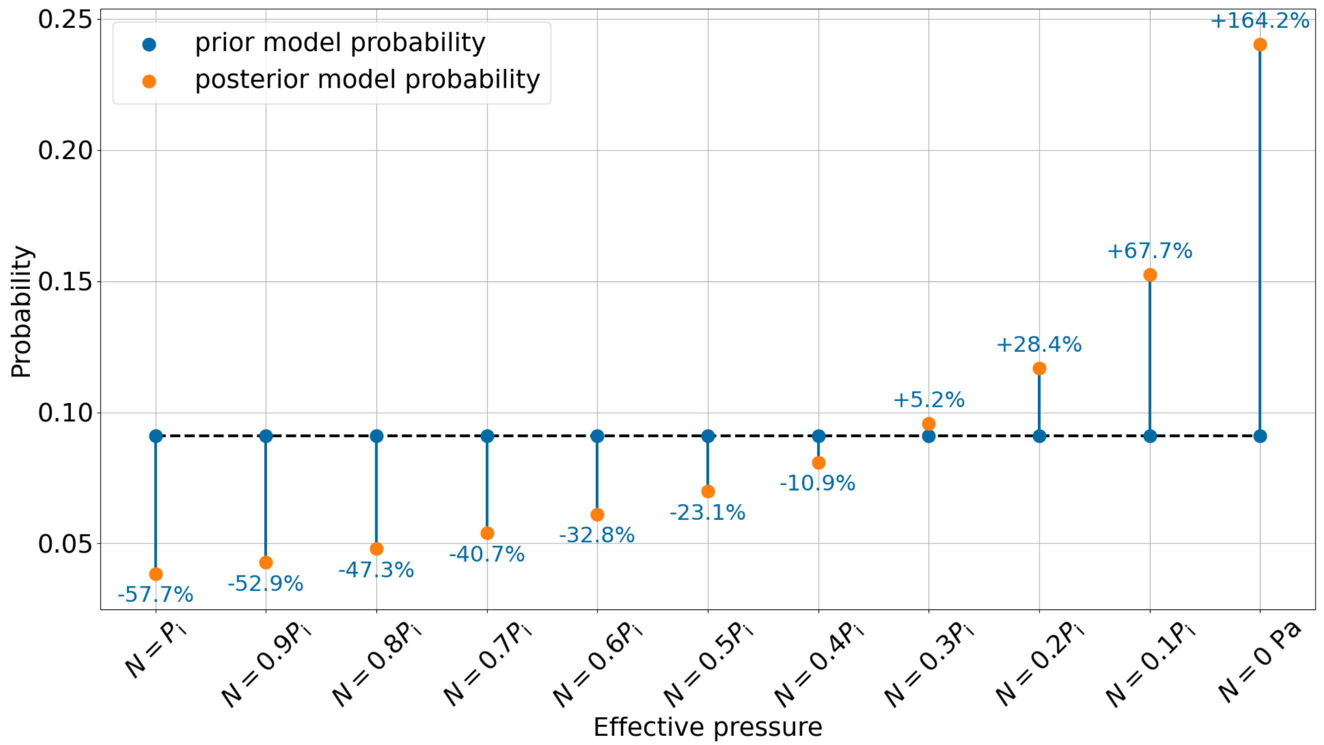

Figure S20. Normalized probabilities given the seismic observations collected on PIG when using different fractions of the overburden pressure, including the two Weertman-type endmember scenarios ($N = 0$ Pa and $N = p_\mathrm{i}$). Otherwise, as Fig. 6 in the main text.

S7 Acoustic impedance for most probable parameters

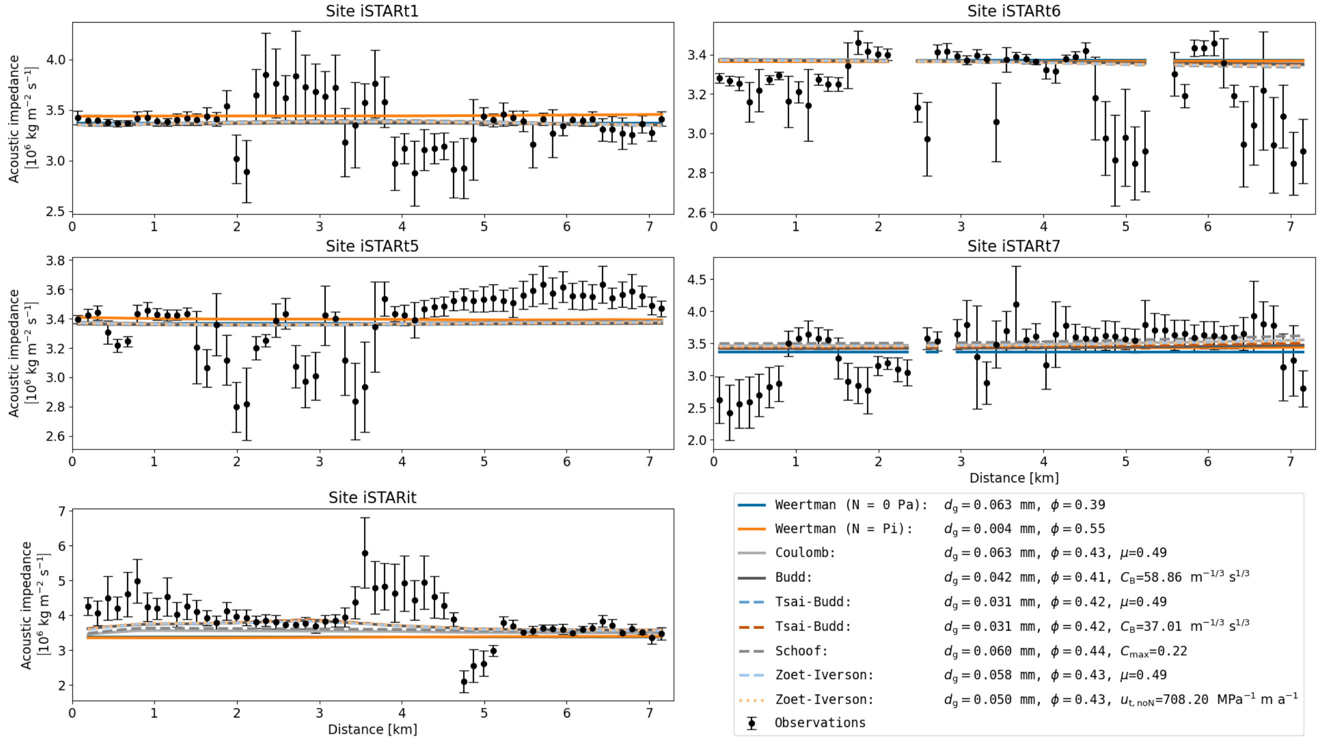

Figure S21. The different panels show the predicted acoustic impedance. For all sliding laws, the acoustic impedance curve is based on the MAP (highest posterior probability) model parameters.

S8 Posterior probabilities for (log-)uniform prior distributions

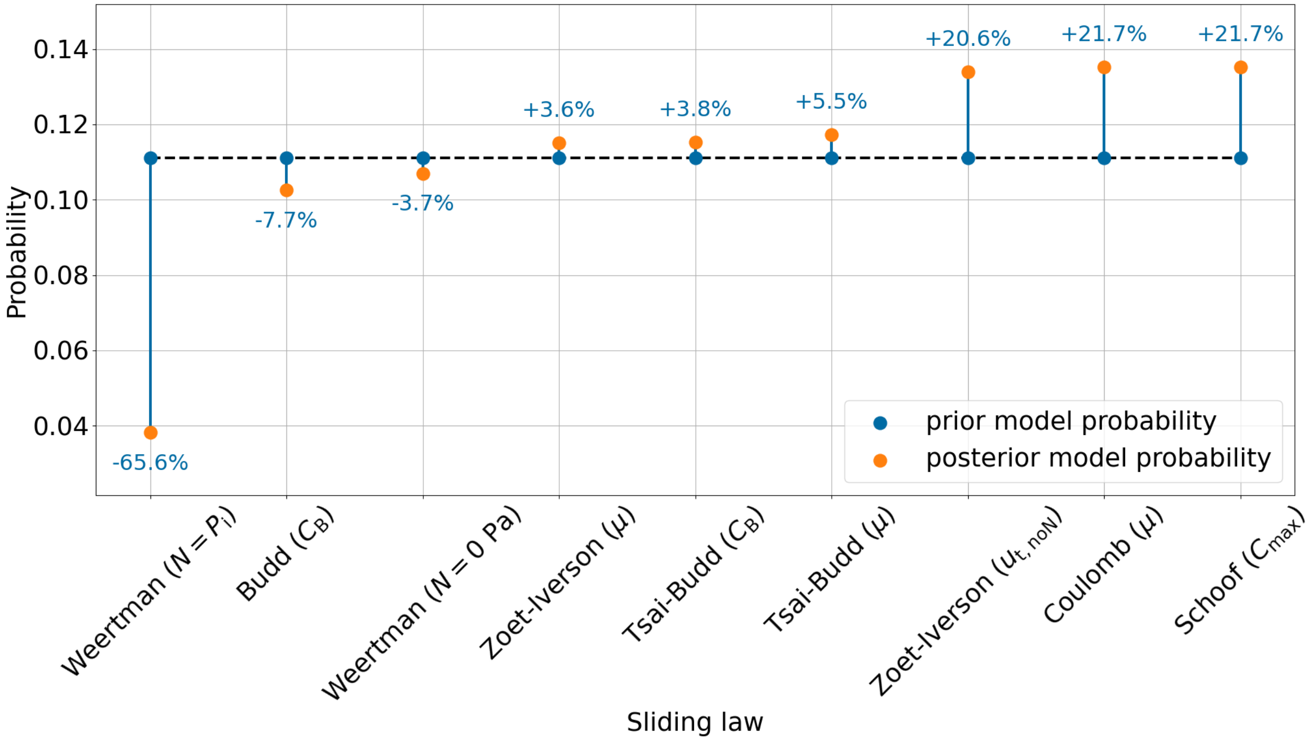

Figure S22. Normalized probabilities of all sliding laws examined in this study given the acoustic impedance observations collected on PIG, and log-uniform prior distributions for scaling coefficients and uniform priors for other parameters. Otherwise, as Fig. 6 in the main text.

S9 Effective pressure for most probable parameters

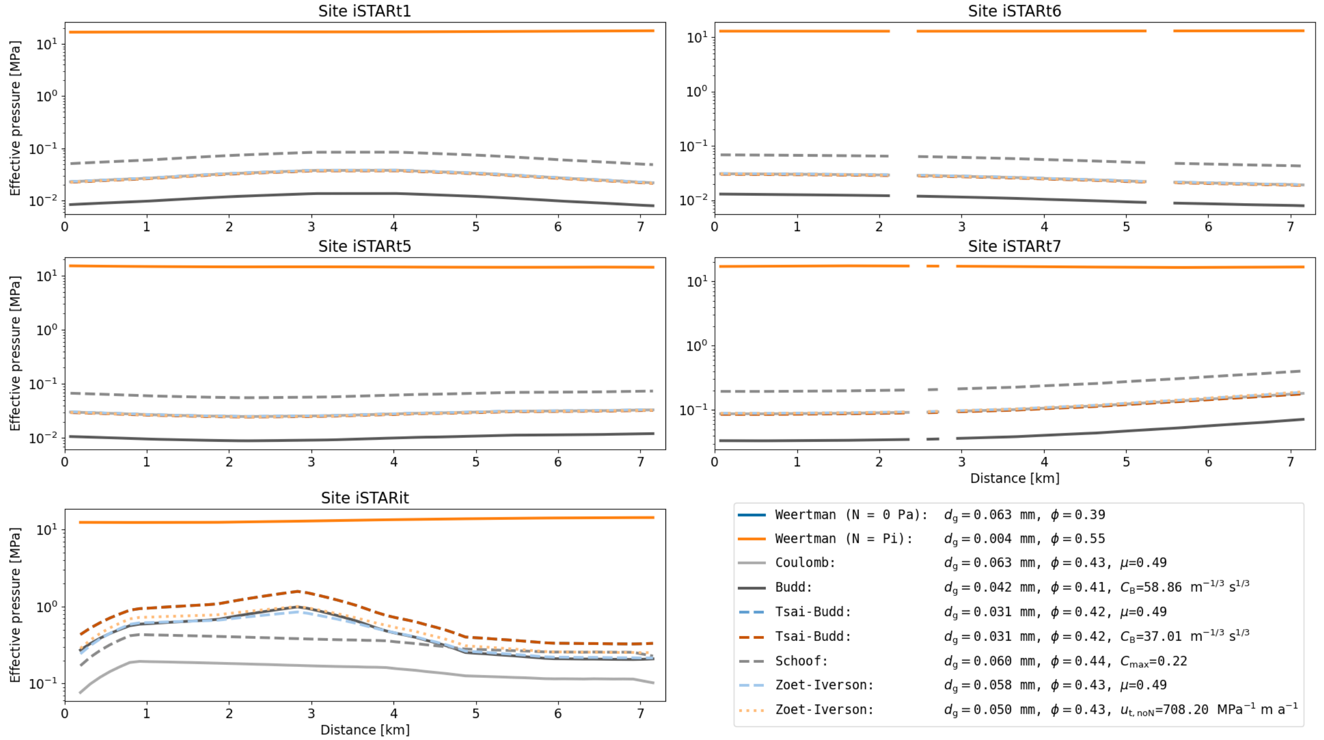

Figure S23. The different panels show the predicted effective pressure. For all sliding laws, the effective pressure curve is based on the MAP (highest posterior probability) model parameters. By definition, the low effective pressure Weertman-type endmember scenario has $N = 0$ Pa and only the MAP parameter values are shown here (not the curve itself). Note the logarithmic scale of the y-axes.

References

Fretwell, P., Pritchard, H. D., Vaughan, D. G., Bamber, J. L., Barrand, N. E., Bell, R., Bianchi, C., Bingham, R. G., Blankenship, D. D., Casassa, G., Catania, G., Callens, D., Conway, H., Cook, A. J., Corr, H. F., Damaske, D., Damm, V., Ferraccioli, F., Forsberg, R., Fujita, S., Gim, Y., Gogineni, P., Griggs, J. A., Hindmarsh, R. C., Holmlund, P., Holt, J. W., Jacobel, R. W., Jenkins, A., Jokat, W., Jordan, T., King, E. C., Kohler, J., Krabill, W., Riger-Kusk, M., Langley, K. A., Leitchenkov, G., Leuschen, C., Luyendyk, B. P., Matsuoka, K., Mouginot, J., Nitsche, F. O., Nogi, Y., Nost, O. A., Popov, S. V., Rignot, E., Rippin, D. M., Rivera, A., Roberts, J., Ross, N., Siegert, M. J., Smith, A. M., Steinhage, D., Studinger, M., Sun, B., Tinto, B. K., Welch, B. C., Wilson, D., Young, D. A., Xiangbin, C., and Zirizzotti, A.: Bedmap2: Improved ice bed, surface and thickness datasets for Antarctica, Cryosphere, 7, 375–393, https://doi.org/10.5194/tc-7-375-2013, 2013.

Graham, A. G., Wåhlin, A., Hogan, K. A., Nitsche, F. O., Heywood, K. J., Totten, R. L., Smith, J. A., Hillenbrand, C. D., Simkins, L. M., Anderson, J. B., Wellner, J. S., and Larter, R. D.: Rapid retreat of Thwaites Glacier in the pre-satellite era, Nature Geoscience, 15, 706–713, https://doi.org/10.1038/s41561-022-01019-9, 2022.